PHYSICAL REVIEW B **96**, 195308 (2017)

Ultrafast optical snapshots of hybrid perovskites reveal the origin of multiband electronic transitions

Kannatassen Appavoo,[1,2] Wanyi Nie,[3] Jean-Christophe Blancon,[4] Jacky Even,[5] Aditya D. Mohite,[3] and Matthew Y. Sfeir[1,*]

[1]*Center for Functional Nanomaterials, Brookhaven National Laboratory, Upton, New York 11973, USA*

[2]*Department of Physics, University of Alabama at Birmingham, Birmingham, Alabama 35233, USA*

[3]*Materials Physics and Application, Los Alamos National Laboratory, Los Alamos, New Mexico 87545, USA*

[4]*Physical Chemistry and Applied Spectroscopy Division, Los Alamos National Laboratory, Los Alamos, New Mexico 87545, USA*

[5]*Fonctions Optiques pour les Technologies de l'Information, FOTON UMR 6082, CNRS, INSA de Rennes, 35708 Rennes, France*

(Received 7 December 2016; revised manuscript received 15 August 2017; published 28 November 2017)

Connecting the complex electronic excitations of hybrid perovskites to their intricate organic-inorganic lattice structure has critical implications for energy conversion and optoelectronic technologies. Here we detail the multiband, multivalley electronic structure of a halide hybrid perovskite by measuring the absorption transients of a millimeter-scale-grain thin film as it undergoes a thermally controlled reversible tetragonal-to-orthogonal phase transition. Probing nearly single grains of this hybrid perovskite, we observe an unreported energy splitting (degeneracy lifting) of the high-energy 2.6 eV band in the tetragonal phase that further splits as the rotational degrees of freedom of the disordered $CH_3NH_3^+$ molecules are reduced when the sample is cooled. This energy splitting drastically increases during an extended phase-transition coexistence region that persists from 160 to 120 K, becoming more pronounced in the orthorhombic phase. By tracking the temperature-dependent optical transition energies and using symmetry analysis that describes the evolution of electronic states from the tetragonal phase to the orthorhombic phase, we assign this energy splitting to the nearly degenerate transitions in the tetragonal phase from both the *R*- and *M*-point-derived states. Importantly, these assignments explain how momentum conservation effects lead to long hot-carrier lifetimes in the room-temperature tetragonal phase, with faster hot-carrier relaxation when the hybrid perovskite structurally transitions to the orthorhombic phase due to enhanced scattering at the Γ point.

DOI: 10.1103/PhysRevB.96.195308

I. INTRODUCTION

Hybrid organic-inorganic perovskites (HOIPs) have emerged as a promising class of materials for solution-processed thin-film photovoltaic [1–4], photodetector [5,6], light-emitting [7,8], and laser [9] technologies. However, to tailor their optoelectronic properties for specific technological applications, it is critical to connect their physical and electronic structures, particularly the role of interactions between the organic and inorganic subunits. The crystal structure typical of HOIPs exhibits an inorganic lead halide $[PbX_6]^{4-}$ (X = I,Cl,Br) subunit in an octahedral three-dimensional crystalline network. Small organic cations (e.g., methyl ammonium) are located in the voids of the ordered octahedral and comprise the organic subunit [Fig. 1(a)]. It has been suggested that the compelling physical properties of these systems, such as the high-absorption cross section [10] and long carrier diffusion length [11,12], that allow for simple planar heterojunction devices with internal quantum efficiencies approaching unity emerge specifically due to this dual organic and inorganic character [13]. However, systematic studies of structure-function properties in hybrid perovskite materials have been hindered by large variability in composition, crystalline quality, and grain size in the literature [11,14–18]. As a result, fundamental scientific questions about the electronic and optical properties of hybrid perovskites remain largely unresolved. Furthermore, the dual organic-inorganic nature results in various interpretations of the free-charge transport mechanism as well, namely, one limited by various opposing mechanisms such as phonon scattering and piezoelectric or space-charge scattering [13]. Understanding these fundamental scientific issues also has practical consequences since there are several factors that contribute to degrading device performance, such as ion migration that leads to hysteresis, formation of trap states and polaronic effects [13,19,20], and light-activated metastable trap states [21].

A comprehensive picture of the complex multiband, multivalley electronic structure [22] is needed to understand the emergence of the unusual optoelectronic properties of HOIP materials, including slow carrier recombination [11,12,23] and suppression of midgap defect states [24–27]. However, the microscopic details that lead to its complex dielectric constant [25,28,29] are not well established, resulting in ambiguities as to the origins of its optical properties [30–32] and leading to a range of reported values for the exciton binding energies and charge-carrier effective masses [33,34]. Even the origin of optical transitions in the visible spectral region remains under debate. Although considerable progress has been made on understanding the fundamental optical transition at ∼1.65 eV [35], including its response during the tetragonal-to-orthorhombic structural phase transition that occurs around 160 K [34], considerable controversy remains regarding the nature of higher-order subband transitions, including whether they result from intrinsic HOIP states [36,37] or an extrinsic charge-transfer-state (I_2-like) species [38]. The higher-energy electronic structure is important, as anomalous hot-carrier lifetimes have been observed in these materials [31,32], suggesting that these effects could be further enhanced for use in hot-carrier-based solar cells [39]. The mechanism for long hot-carrier lifetimes is still poorly understood, with

*Corresponding author: msfeir@bnl.gov

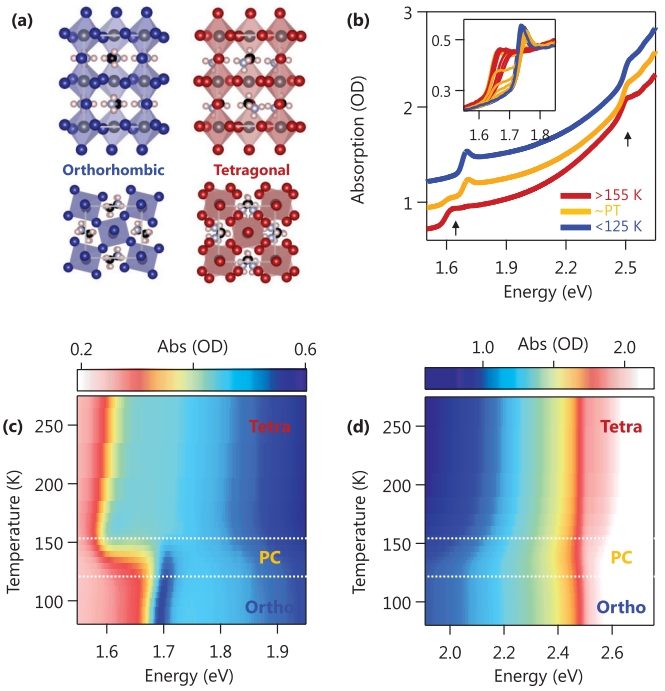

FIG. 1. Steady-state linear optical properties of hybrid organic-inorganic perovskite. (a) Crystal structure of the HOIP in its orthorhombic (low-temperature phase, blue) and tetragonal (high-temperature phase, red) state. (b) Characteristic linear absorption spectra before, during, and after the phase transition. The inset represents spectra taken at all temperature points. (c) and (d) Two-dimensional absorption spectra as a function of temperature in the visible and near-infrared spectral regions. Note change of color scale. Region depicting phase coexistence is marked by white dotted lines.

potential contributions from a phonon bottleneck [31,32], a spin (Rashba) effect [40–43], or a density-of-states effect [44,45]. The long hot-carrier lifetimes may also contribute to the long carrier diffusion lengths and overall charge-carrier lifetimes obtained in these materials despite the modest carrier mobilities that have been measured [20,46].

To address issues related to reproducibility and quality, Nie *et al.* have recently demonstrated that a hot-casting fabrication technique yields millimeter-grain-size high-quality thin films of hybrid perovskite material. In contrast to other synthetic approaches, these thin films yield consistent, hysteresis-free solar-cell devices with efficiencies approaching 18% [21]. The improved performance is attributed to the formation of large grains that reduce bulk defects and increase charge-carrier mobilities [$\sim$20 $cm^2/(V\,s)$ for a grain size of 170 μm] [4]. These large grain sizes in hybrid perovskite thin films reduce the effect of grain boundaries that can locally modify the motion of organic molecules due to space-charge effects, allowing optical measurements to be carried out at the near-single-grain level. While the improvement in the device characteristics of these large-grain thin-film samples has been well established [4,21,26], corresponding high-sensitivity optical studies have not been similarly reported.

Here we take advantage of this hot-casting fabrication approach to produce high-quality, millimeter-scale grains of methylammonium lead iodide ($MAPbI_3$) thin films and to study the properties of electronic excitations at the near-single-domain level [4], with minimal influence of grain boundaries. First, we assign the set of optical transitions in the visible and near infrared using variable-temperature transient absorption measurements, which provide a sensitive probe of the electronic energy levels in addition to elucidating carrier dynamics. In the room-temperature tetragonal phase, we observe two nearly degenerate optical transitions near 2.6 eV originating from different momentum states. When homogeneous broadening associated with rotation of the organic cation is suppressed, these distinct transitions are clearly resolved. In the low-temperature (low-T) orthorhombic phase, the energy splitting between these higher subband transitions is enhanced. The observed structural phase transition is not abrupt but, instead, exhibits a rather large phase-coexistence region spanning tens of degrees, during which a large increase in electron-phonon coupling that primarily affects the higher subbands is observed. We use Brillouin zone folding concepts to assign the higher-subband optical transitions near 2.6 eV as well as the appearance of a weak absorption feature at $\sim$2 eV in the orthorhombic phase. Furthermore, using these concepts, we explain the dramatic changes in the hot-carrier cooling rates between the two structural phases.

II. OBSERVATION OF A BROAD PHASE-COEXISTENCE REGION

Linear optical measurements on a millimeter-sized grain were made using a high-brightness Fourier-transform-based spectrometer describe previously [47]. These methylammonium lead iodochloride thin films (herein referred to as hybrid perovskite or HOIP) were fabricated on sapphire substrates using our previously developed hot-casting method with PbI_2 and MACl (1:1) precursor in Dimethylformamide (DMF) [4]. For all measurements, samples were mounted in a helium flow optical cryostat and pumped down to 10^{-6} Torr. These measurements reveal features similar to perovskite samples grown using various fabrication techniques, indicating that grain boundaries only weakly influence the primary absorption features. For example, we can use linear optical measurements to determine that a structural phase transition occurs near 160 K, where the $[PbX_6]^{4-}$ octahedron realigns itself to form an orthorhombic structure while the $CH_3NH_3^+$ molecules collectively align themselves by coupling to the distortion of the inorganic network. Like in previous reports [34], the onset of near-infrared (NIR) absorption at $\sim$1.6 eV ($\sim$775 nm) blueshifts and becomes more prominent in the low-temperature orthorhombic phase compared to the room-temperature tetragonal phase [Fig. 1(b), inset] [30,48]. Although we readily observe changes in the low-energy electronic structure [Fig. 1(c)], changes at higher energies, including excitonic features associated with other subbands, are difficult to discern [Fig. 1(d)]. Instead, broad featureless transitions within the continuum states dominate the optical absorption and are relatively insensitive to changes in the physical and electronic structure.

However, we can establish a detailed picture of the multivalley optical absorption and relaxation processes using variable-temperature ultrafast transient optical spectroscopy. Broadband transient absorption measurements of our HOIP films

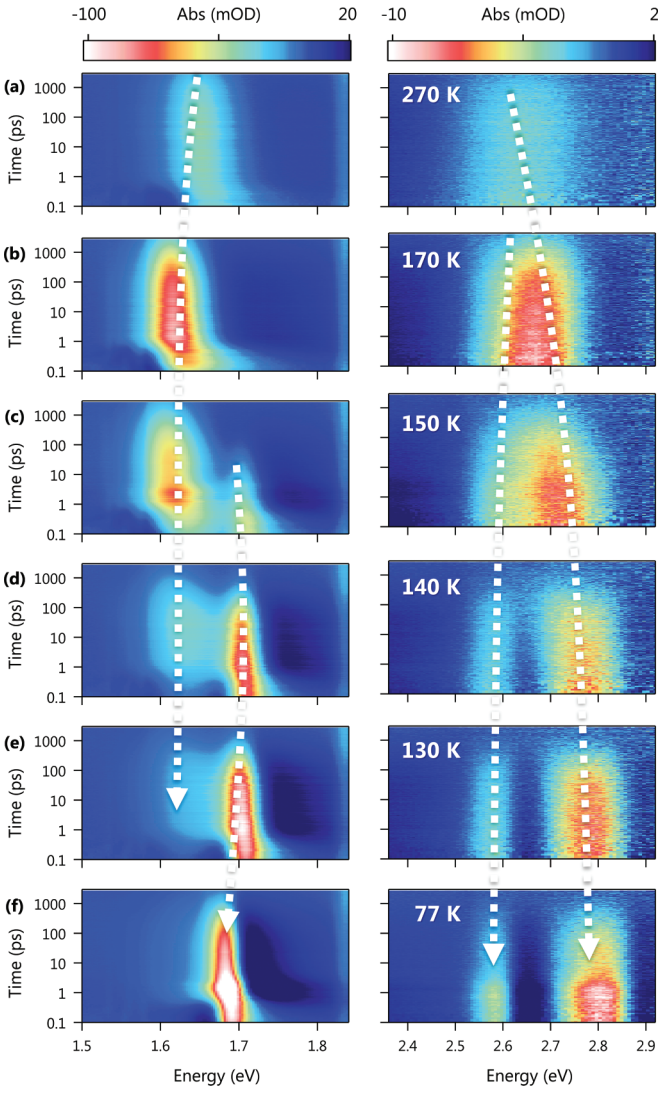

FIG. 2. Temperature-dependent ultrafast dynamics of hybrid perovskite. Broadband transient absorption dynamics for optical pumping at 1.9 eV at key temperature points. Both the high-temperature tetragonal phase and the low-temperature orthorhombic phase can be observed over a wide phase-coexistence region. In addition to the abrupt blueshift of the ∼1.7 eV low-energy peak, the orthorhombic phase is characterized by a splitting of the high-energy optical transition at 2.7 eV. White lines are guides to the eyes to track bands relevant to our discussion.

at several key temperatures are shown in Fig. 2 for excitation with a low-energy pump pulse ($<5\ \mu J/cm^2, \lambda = 650$ nm, pulse duration of ∼100 fs). Our transient spectra in the tetragonal phase [Fig. 2(a)] are dominated by narrow ground-state bleach signals at ∼1.6 eV(750 nm), previously assigned to a transition between the valence-band maxima (VB_1) and conduction band minima (CB_1) at the R point [49], and a higher-energy ground-state bleach signal ($\Delta A < 0$) at ∼2.64 eV (470 nm) whose origin is still controversial [36–38]. These ground-state bleach signals originate from a modification of the exciton transition matrix elements by photoexcited free carriers rather than real population of excitonic states [31,36]. The high oscillator strength of the excitons compared to the continuum transitions allows us to identify features that are obscured in linear optical measurements [31,38]. The virtual excitonic signal can be directly compared to experimental conditions in which we used higher-photon-energy pulses (>2.6 eV) to directly populate those higher subbands (discussed below and in the Supplemental Material [50]). The transient spectra associated with the orthorhombic phase [Fig. 2(f)] have received less attention, with most experimental data focusing on the low-energy peak at 1.7 eV [51]. In contrast to the tetragonal phase, we now observe two peaks at ∼2.6 and 2.8 eV that decay identically to each other. We note that the systematic appearance of these two distinct optical transitions when the material undergoes its characteristic phase transition is also observed in bulk single-HOIP crystals (Supplemental Material [50]) and is therefore an intrinsic property of the HOIP material. These narrow excitonic features associated with each subband allow us to detect minute changes in the electronic structure as the HOIP undergoes its thermally controlled structural phase transition.

In contrast to previous absorption-based studies [34], our samples show a large temperature range over which the orthorhombic and tetragonal phases coexist [Figs. 2(c)–2(e)]. This phase coexistence occurs from around 160 to 120 K, during which transient features characteristic of both phases are simultaneously observed. Spectral and temporal discrimination in transient measurements allows us to detect the minority species of tetragonal sites that persist at temperatures considerably lower than the nominal phase-transition temperature [Figs. 2(c)–2(e)], even though their contribution to the linear spectra is too small to be clearly observed. To highlight the evolution of the absorption features, we plot a series of spectra extracted 5 ps after photoexcitation at temperatures ranging from 270 to 77 K (Fig. 3). The phase-coexistence region corresponds to the yellow curves in Figs. 3(c) and 3(d). For the low-energy transition, the tetragonal phase contributes a peak at 1.6 eV, and the orthorhombic phase contributes a peak at ∼1.7 eV, such that both peaks are readily observed in the phase-coexistence region, but only one peak is observed in either phase. This observation is consistent with reports that residual tetragonal islands exist within the orthorhombic crystal structure of the hybrid perovskite at temperatures considerably lower than the phase-transition point (160 K) [18,48,52–54]. Taken together, these results imply that the phase-coexistence region is a universal feature of these materials, but the width of the temperature range will depend on the details of the material's morphology. The data are more complex for the higher-energy feature at ∼2.7 eV. Here two peaks are seen in both the phase-coexistence region and the low-temperature orthorhombic phase, with an energy splitting that increases with decreasing temperature. As such, we conclude that these two peaks correspond to distinct optical transitions whose energy separation is enhanced in the lower-symmetry orthorhombic phase.

III. PEAK SPLITTING IN THE TETRAGONAL PHASE

Furthermore, close examination of the variable-temperature transient spectra in the tetragonal phase reveals that two distinct peaks can be resolved even at temperatures well *above* the phase transition. At around 250 K and for lower temperatures, the seemingly single broadened feature in the

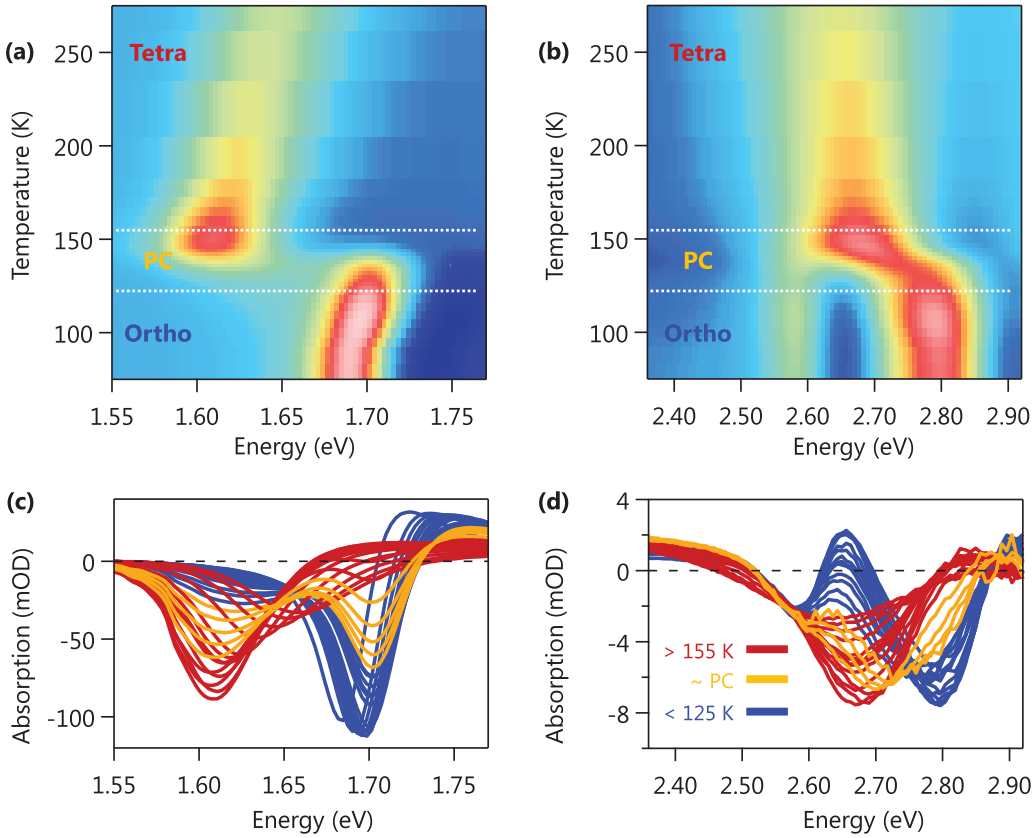

FIG. 3. Ultrafast electronic excitations as coupled to the structural phase transition. Spectral slices of the ultrafast transient absorption data taken at 5 ps and plotted as a function of temperature. These two-dimensional spectra are plotted in the visible and near-infrared regions. White lines mark the coexistence between the two phases as observed in the ultrafast data.

tetragonal phase at ∼2.6 eV splits into two distinct but overlapping narrow ground-state bleaches (red curves in Fig. 3, with details on curve fitting in the Supplemental Material [50]). Notably, the temperature at which this splitting first becomes apparent corresponds to suppression of the methyl and/or ammonium rotation around the C-N axis, as evidenced by recent neutron scattering experiments [55,56]. As such, we conclude that the free rotation of the methyl and/or ammonium groups that occurs at room temperature effectively obscures differences between these high-energy absorption bands, yielding an effectively broadened single peak. We note that stable photovoltaic cells fabricated from these materials perform without degradation for extended hours when operated close to 250 K [21]. We observe no other notable spectral or dynamical change at this temperature, suggesting that inhibiting these molecular motions while preserving this intra-unit-cell dipolar interaction may be key to better device performance. As the phase transition proceeds to the orthorhombic phase, the splitting of the bands becomes more prominent, evolving into two distinct peaks at ∼2.58 eV (480 nm) and ∼2.80 eV (440 nm). From our fits, we determine that the high-energy subbands are separated by a maximum of ∼75 meV in the tetragonal structure and that the separation increases to ∼230 meV in the orthorhombic state. As discussed below, we determine that the splitting of the visible absorption band in the two phases has a common origin and the increase in energy separation is a direct consequence of the phase transition that modifies the unit-cell size and allows greater organic-inorganic interaction.

IV. ANALYSIS OF TEMPERATURE-DEPENDENT ELECTRONIC STATES

The temperature-dependent optical transition relationship (dE/dT) provides finer details of the coupling mechanism between the organic (CH_3NH_3) and the inorganic (PbX_3 octahedra) sublattices, as detailed below. Furthermore, we are able to identify temperature–dependent effects within a given phase as well as the origins of the discontinuities that occur at the critical phase-transition temperature. These optical transition energies as a function of temperature show a complex pattern, with distinct dE/dT values for the different subband transitions and different phases [Fig. 4(a)]. The temperature dependence of the energy levels, i.e., dE/dT, originates from various effects and can be written as [57–59]

$$\left(\frac{dE}{dT}\right) = \left(\frac{\partial E}{\partial T}\right)_{\text{lattice}} + \left(\frac{\partial E}{\partial T}\right)_{\text{strain}} + \left(\frac{\partial E}{\partial T}\right)_{\substack{\text{el-ph}\\ \text{coupling}}}.$$

In this equation, $(\frac{\partial E}{\partial T})_{\text{strain}}$ can be safely ignored as it is related to mechanical strain effects that are relaxed in thin films. Such a contribution, if present, would have typical values that are only in the few tens of μeV, instead of the values spanning hundreds to thousands of μeV obtained in our case. However,

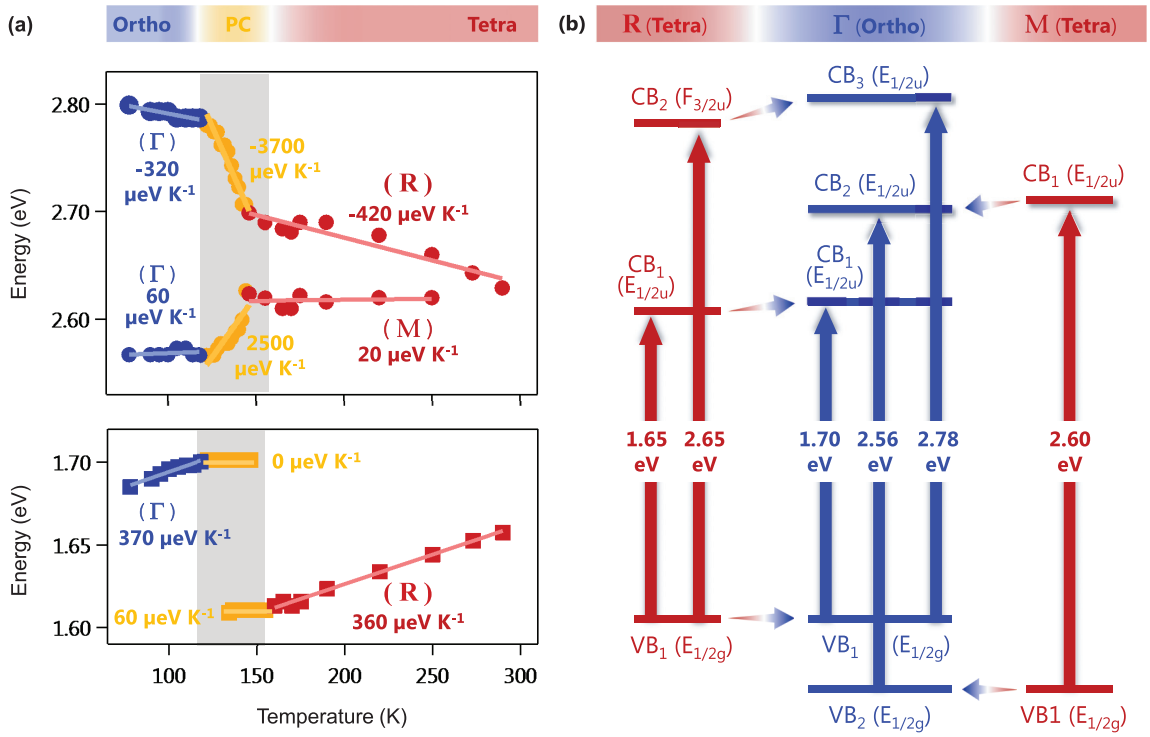

FIG. 4. Energy of optical transitions in hybrid perovskite as a function of temperature. (a) Peak energy positions obtained from ultrafast transient absorption data as a function of temperature. Red, yellow, and blue represent the tetragonal phase, phase coexistence, and the orthorhombic phase, respectively. (b) Schematic of the optical transitions and symmetry labels of the hybrid perovskite showing the origins of the various optical transitions in both phases. We note that $VB_1(R)$-$CB_2(R)$ is similarly allowed and nearly degenerate with $VB_1(M)$-$CB_1(M)$. For simplicity, labels for the irreducible representations of the cubic phase are used to describe the tetragonal phase. A complete description of these bands is given in the Supplemental Material [50].

for the case of the bulk $MAPbI_3$ single crystal studied (results shown in the Supplemental Material [50]), mechanical strain effects are clearly seen as this results in smearing of the otherwise sharp ultrafast electronic transition features. The remaining terms, $(\frac{\partial E}{\partial T})_{\text{lattice}}$ and $(\frac{\partial E}{\partial T})_{\substack{\text{el-ph} \\ \text{coupling}}}$, represent thermal expansion/contraction of the lattice and the electron-phonon coupling, respectively, and are typically on the order of a few hundred μeV.

Above and below the structural phase transition, the electronic evolution is consistent with lattice effects being the dominant term. However, within the phase-coexistence region, the electronic evolution with temperature shows a distinct behavior that is best explained by significant changes in electron-phonon coupling. The transient bleach signal in the NIR behaves similarly to the linear spectra, exhibiting a systematic redshift until the critical temperature is reached, where an abrupt blueshift of ~40 nm occurs [see Fig. 1(c) for linear measurements, and Figs. 3(a) and 4(a) for transient measurements]. From Fig. 4(a), the NIR optical transition exhibits a similar positive slope in both phases (~360 μeV/K in the tetragonal state and ~370 μeV/K in the orthorhombic state) that corresponds to normal thermal expansion of the lattice. We note that these values are similar to those obtained for lead salts [57] and are ~100 μeV/K greater than a previous measurement performed on small grains [51] (but still within ~30% of the bulk values [51]). This is due to the enhanced crystallinity of our large-grain HOIP that leads to a reduced value for defect density and a greater effect when the lattice expands with increased temperature. However, the two closely spaced absorption peaks in the visible range exhibit drastically different temperature-dependent optical transitions behaviors. The dE/dT values for the highest-energy visible peak (~2.65 eV in the tetragonal phase and ~2.8 eV in the orthorhombic phase) are similar to those for the NIR transition but with negative values for the slope. This implies a complementary motion within the hybrid perovskite sublattice, potentially as the orbital overlap within the inorganic $[PbX_6]^{4-}$ cage is modified. Interestingly, the lower-energy visible absorption feature at ~2.6 eV is nearly temperature independent and has an energy that differs by only ~50 meV between the two structural phases, highlighting minimal interaction between the dipolar $CH_3NH_3^+$ and the asymmetric unit cell as defined by the $[PbX_6]^{4-}$ octahedral cage.

Importantly, the temperature-dependent optical transitions within the extended phase-coexistence region are distinct from the behavior in either phase. This allows us to differentiate between electronic effects induced by the structural reorganization of the inorganic and organic subunits. For the low-energy band edge (~1.65 eV), dE/dT is almost zero in the phase-coexistence region. As this absorption is associated with the R point in reciprocal space, where we expect the organic molecule to play a minimal role [25], a featureless $|dE/dT|$ during the phase transition is expected and corresponds to negligible changes in the I $5p$ orbital

overlap with the orbitals of the organic subunit [25]. More striking is the temperature dependence of the higher subbands within the phase-coexistence regime [Fig. 4(a), yellow region], where dE/dT values are about ten times greater than those in either the orthorhombic or tetragonal region. Lattice expansion/contraction cannot account for the large $|dE/dT|$ values observed (∼2500 and ∼3700 μeV/K), implying a different mechanism that shifts the energy levels. Instead, this drastic $|dE/dT|$ change is assigned to large systematic changes in electron-phonon coupling due to enhanced electronic interactions between the organic and inorganic subunits at higher energy. This interpretation is consistent with electronic structure calculations that indicate that contributions of the organic orbitals become non-negligible at photon energies above 2 eV, including the effect of charge localization on nitrogen atoms [25,53]. It is also possible that the coexistence of the tetragonal and orthorhombic phases also contributes to this phenomenon, influencing how the organic $CH_3NH_3^+$ molecules interact with the distorted $[PbX_6]^{4-}$ octahedral cage. We note that the opposite signs of $(\frac{\partial E}{\partial T})_{\text{coupling}}^{\text{el-ph}}$ for the 2.6 and 2.8 eV optical transitions is consistent with the fact that these contributions can be positive or negative depending on the subband and the nature of the coupling [59,60].

V. ASSIGNMENT OF OPTICAL TRANSITIONS USING SYMMETRY ANALYSIS

To understand the evolution of the HOIP electronic structure from the tetragonal to orthorhombic phase, including the electronic energy-level splitting and the temperature-dependent optical transition behavior, we use a zone-folding concept based on symmetry analysis, similar to what was recently used to analyze the cubic-to-tetragonal phase transition [22]. We note that the R-point transitions of the cubic phase are actually folded to the Γ point in the tetragonal phase, but for clarity, we have kept the irreducible representations and Brillouin zone of the pseudocubic perovskite $Pm\ 3m$ reference phase when discussing the tetragonal phase. The optical transitions in the tetragonal phase are assigned using density functional theory calculations of the imaginary part of the dielectric function for the high-T cubic phase of HOIP within the random-phase approximation [49], which match experimental determinations of the absorption onset [12]. These calculations suggest that the primary absorption features correspond to an R-point transition at the band gap energy (1.65 eV) and a set of symmetry-allowed transitions involving both the R and M points at ∼1 eV higher energy [37]. The same conclusion concerning the energetic positions of the bands has been drawn from refined density functional theory computations of the electronic band diagrams [29], including many-body corrections at the GW level [28,61,62]. The band-folding concept clarifies the seeming complexity of the band diagram in the low-T *Pnma* phase [22,50].

This analysis allows us to assign the higher-subband optical transitions in these materials to an accidental degeneracy involving both $VB_1(R)$ -$CB_2(R)$ [as well as $VB_2(R)$-$CB_1(R)$, not shown in Fig. 4(b)] and $VB_1(M)$-$CB_1(M)$ transitions [37]. As the unit-cell size increases by a factor of 4 ($Z = 4$) in a cubic-to-tetragonal/orthorhombic phase (*Pnma*), the Brillouin zone volume reduces by a factor of 4. The electronic states close to the electronic band gap are folded at low temperature from the R and M points of the cubic/tetragonal phase Brillouin zone to the Γ point of the orthorhombic supercell Brillouin zone [22] [Fig. 4(b)]. For example, the measured band gap in the low-T orthorhombic phase is equal to about 1.70 eV (730 nm) and is attributed to folding of the tetragonal $VB_1(R)$-$CB_1(R)$ transition to $VB_1(\Gamma)$-$CB_1(\Gamma)$. The next allowed higher-subband transitions in the tetragonal phase include $VB_1(R)$-$CB_2(R)$ [$VB_2(R)$-$CB_1(R)$] and $VB_1(M)$-$CB_1(M)$ [28,37,49]. In the orthorhombic phase, both of these transitions are folded to the Γ point and are still allowed by symmetry. Indeed, we observe these two transitions in both the orthorhombic and tetragonal phases, where they become observable below 250 K when the homogeneous broadening associated with motion of the methylammonium ions are suppressed. Furthermore, these assignments are supported by dE/dT data. The nearly flat temperature-dependent optical transition at ∼2.6 eV is consistent with an M-point-derived transition, while the dE/dT associated with the R-point-derived transition at ∼2.8 eV has a magnitude similar to that of the band edge (R-point) transition.

VI. CONSEQUENCES FOR THE HOT-CARRIER DYNAMICS

The hot-carrier lifetimes decrease in the orthorhombic phase, in support of the zone-folding picture in which all the relevant allowed optical transitions originate from the Γ point. Pumping the tetragonal phase at 2.95 eV results in occupation of energy levels associated with the M point transition [Fig. 5(a)]. This is seen clearly by inspection of the transient spectra, which exhibit an additional sharp feature at ∼2.5 eV [compared to data in Fig. 2(a)] and which exhibit distinct decay kinetics relative to the virtual signal at 2.64 eV. As seen in the middle panel of Fig. 5(a), the sharp peak at 2.5 eV contains an additional decay component that extends over several tens of picoseconds. Interestingly, the measured decay time constant (∼40 ps) is similar to a previously assigned decay component in transient photoluminescence measurements under similar pump conditions that was attributed to dynamic coupling of the organic and inorganic sublattices [53]. This hot-carrier lifetime is of the same order as recently studied thin films of other hybrid perovskites [13,31,32,63–65] and longer than in other hot-carrier-based systems like plasmonics [66–69] and quantum dots and nanocrystals [70–73] with values typically less than 10 ps.

In contrast, when pumping the orthorhombic phase at 2.95 eV, we find that the 2.55 and 2.76 eV features decay identically to each other and similarly to the primary ground-state bleach feature at 1.7 eV. The features associated with the higher subbands do not contain an additional decay component associated with a long-lived hot carrier [Fig. 5(b), middle panel]. We interpret the rapid hot-carrier decay in the orthorhombic phase as arising from alignment of the optical transitions in momentum space due to zone folding that leads to an enhanced scattering rate, efficiently relaxing hot carriers from high-energy subbands to the band edge. Notably, in the tetragonal phase, the M-point hot-carrier feature (2.5 eV) decays slower than the sharp photoinduced

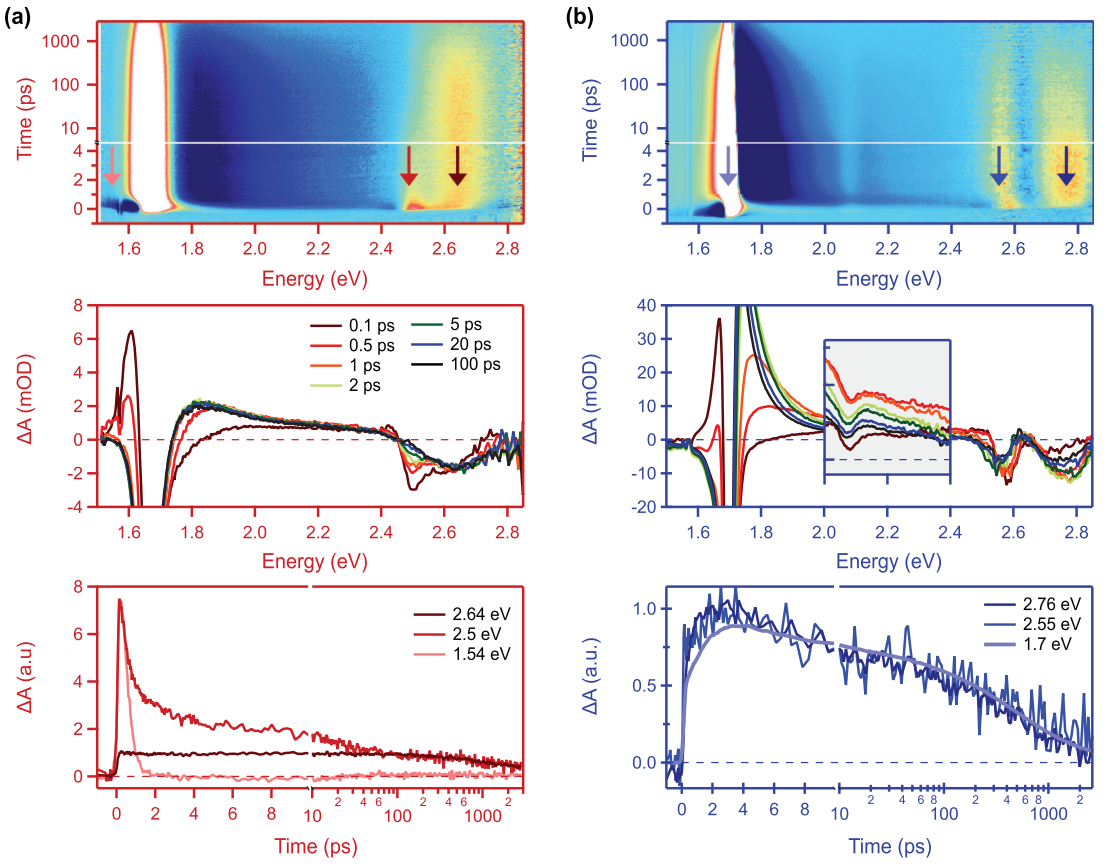

FIG. 5. Hot-carrier dynamics in different structural phases. (a) Top: Raw transient absorption data for the high-temperature tetragonal phase for optical pumping at 2.95 eV. Middle: Transient spectra extracted at a few time points showing that hot carriers modify the features associated with both 1.65 and 2.6 eV optical transitions. Bottom: The kinetic traces (normalized relative to the peak of the 2.64 eV decay) for probed photon energies, reflecting the occupation of a higher-energy subband associated with the 2.5 eV transition for times exceeding 10 ps. (b) Top: Transient absorption data for the low-temperature orthorhombic phase for optical pumping at 2.95 eV. Middle: Transient spectra extracted at a few time points show that hot carriers predominantly affect the 1.7 eV optical transition. The inset expands the ΔA range from -1 to 8 milli Optical Density to emphasize the appearance of a new ground-state bleach feature at 2.05 eV. Bottom: The normalized kinetic traces for probe photon energies show that the 2.76 and 2.55 eV peaks exhibit relaxation dynamics similar to that of the main ground-state bleach signal at 1.7 eV; that is, no significant hot-carrier population persists in higher-energy subbands.

absorption signal at 1.54 eV. The evolution of the primary NIR transition has been previously used as a marker for hot-carrier lifetimes [31,32], but our results imply that it does not reflect hot-carrier populations in all subbands. We also note that recent suggestions of a charge-transfer-state (I_2-like) species as the origin of the optical feature at ∼480 nm are incompatible with our results [38]. Indeed, the ability to repeatedly and reproducibly use the HOIP structural phase transition to interrogate these higher-energy subbands precludes the idea of PbI_2 as a major contributor to this signal.

Crossed optical transitions involving simultaneously M-point and R-point electronic states, that is, originating from the tetragonal $VB_1(M)$-$CB_1(R)$ and $VB_1(R)$-$CB_1(M)$ states, are now allowed in the orthorhombic phase since all VB (CB) states belong to the same $E_{1/2g}(E_{1/2u})$ irreducible representations. These transitions now correspond to $VB_1(\Gamma)$-$CB_2(\Gamma)$ and $VB_2(\Gamma)$-$CB_1(\Gamma)$ in Fig. 4(b), with computed oscillator strengths that amount to, respectively, 5% and <1% of the primary transitions, with calculated energies (2.05 and 2.35 eV) that are intermediate between the two primary transitions observed in the experiment. However, we note that transient absorption measurements [inset in Fig. 5(b)] in the orthorhombic phase do exhibit a very weak ground-state bleach feature near 2.05 eV that is not observed in the tetragonal phase. We assign this peak to the crossed transition originating from the tetragonal $VB_1(M)$-$CB_1(R)$ states because of correspondence to its predicted transition energy.

VII. CONCLUSION

We combined ultrafast transient absorption with a detailed symmetry analysis to assign the multivalley origin of electronic transitions in hybrid organic-inorganic perovskite materials. We demonstrated that the high-energy absorption near 2.6 eV consists of two distinct, albeit nearly degenerate, transitions that are associated with the M and R points of a pseudocubic unit cell. The momentum mismatch between the M-point-derived state and the band edge state leads to a long-lived hot-carrier population in the tetragonal state. In the orthorhombic state, hot carriers from these higher subbands relax much faster

to the band edge since this momentum mismatch does not exist. The observed energy splitting between M- and R-point-derived states is an intrinsic effect that we observe for both thin films and bulk single crystals. These results attest to the exceptional quality of these millimeter-scale-grain thin films that also show the benefit of reduced strain (narrow linewidths) and high tolerance to thermal cycling of the tetragonal-to-orthogonal phase transition.

ACKNOWLEDGMENTS

The work at Los Alamos National Laboratory (LANL) was supported by DOE Office of Basic Energy Sciences Work Proposal 08SPCE973 (W.N., J.-C.B., and A.D.M.) and by the LANL LDRD program (A.D.M.). This work was performed, in part, at the Center for Integrated Nanotechnologies, an Office of Science User Facility operated for the U.S. Department of Energy (DOE) Office of Science. Los Alamos National Laboratory, an affirmative action equal opportunity employer, is operated by Los Alamos National Security, LLC, for the National Nuclear Security Administration of the U.S. Department of Energy under Contract No. DE-AC52-06NA25396. (J.E.). J.E.'s work was also supported by University of Rennes 1 (Action Incitative, Défis Scientifique Emergents 2015) and the Fondation d'entreprises banque Populaire de l'Ouest under Grant No. PEROPHOT 2015. This research used resources of the Center for Functional Nanomaterials, which is a U.S. DOE Office of Science Facility, at Brookhaven National Laboratory under Contract No. DE-SC0012704.

[1] M. M. Lee, J. Teuscher, T. Miyasaka, T. N. Murakami, and H. J. Snaith, Science **338**, 643 (2012).
[2] J. Burschka, N. Pellet, S.-J. Moon, R. Humphry-Baker, P. Gao, M. K. Nazeeruddin, and M. Graetzel, Nature (London) **499**, 316 (2013).
[3] H. J. Snaith, J. Phys. Chem. Lett. **4**, 3623 (2013).
[4] W. Nie, H. Tsai, R. Asadpour, J.-C. Blancon, A. J. Neukirch, G. Gupta, J. J. Crochet, M. Chhowalla, S. Tretiak, M. A. Alam, H.-L. Wang, and A. D. Mohite, Science **347**, 522 (2015).
[5] Q. Lin, A. Armin, P. L. Burn, and P. Meredith, Nat. Photonics **9**, 687 (2015).
[6] S. Yakunin, M. Sytnyk, D. Kriegner, S. Shrestha, M. Richter, G. J. Matt, H. Azimi, C. J. Brabec, J. Stangl, M. V. Kovalenko, and W. Heiss, Nat. Photonics **9**, 444 (2015).
[7] Z.-K. Tan, R. S. Moghaddam, M. L. Lai, P. Docampo, R. Higler, F. Deschler, M. Price, A. Sadhanala, L. M. Pazos, D. Credgington, F. Hanusch, T. Bein, H. J. Snaith, and R. H. Friend, Nat. Nanotechnol. **9**, 687 (2014).
[8] S. D. Stranks and H. J. Snaith, Nat. Nanotechnol. **10**, 391 (2015).
[9] H. Zhu, Y. Fu, F. Meng, X. Wu, Z. Gong, Q. Ding, M. V. Gustafsson, M. T. Trinh, S. Jin, and X. Y. Zhu, Nat. Mater. **14**, 636 (2015).
[10] S. De Wolf, J. Holovsky, S.-J. Moon, P. Löper, B. Niesen, M. Ledinsky, F.-J. Haug, J.-H. Yum, and C. Ballif, J. Phys. Chem. Lett. **5**, 1035 (2014).
[11] S. D. Stranks, G. E. Eperon, G. Grancini, C. Menelaou, M. J. P. Alcocer, T. Leijtens, L. M. Herz, A. Petrozza, and H. J. Snaith, Science **342**, 341 (2013).
[12] G. Xing, N. Mathews, S. Sun, S. S. Lim, Y. M. Lam, M. Grätzel, S. Mhaisalkar, and T. C. Sum, Science **342**, 344 (2013).
[13] X. Y. Zhu and V. Podzorov, J. Phys. Chem. Lett. **6**, 4758 (2015).
[14] D. Shi, V. Adinolfi, R. Comin, M. Yuan, E. Alarousu, A. Buin, Y. Chen, S. Hoogland, A. Rothenberger, K. Katsiev, Y. Losovyj, X. Zhang, P. A. Dowben, O. F. Mohammed, E. H. Sargent, and O. M. Bakr, Science **347**, 519 (2015).
[15] C. C. Stoumpos, L. Frazer, D. J. Clark, Y. S. Kim, S. H. Rhim, A. J. Freeman, J. B. Ketterson, J. I. Jang, and M. G. Kanatzidis, J. Am. Chem. Soc. **137**, 6804 (2015).
[16] X. Wu, M. T. Trinh, D. Niesner, H. Zhu, Z. Norman, J. S. Owen, O. Yaffe, B. J. Kudisch, and X. Y. Zhu, J. Am. Chem. Soc. **137**, 2089 (2015).
[17] J.-H. Im, I.-H. Jang, N. Pellet, M. Grätzel, and N.-G. Park, Nat. Nanotechnol. **9**, 927 (2014).
[18] D. Li, G. Wang, H.-C. Cheng, C.-Y. Chen, H. Wu, Y. Liu, Y. Huang, and X. Duan, Nat. Commun. **7**, 11330 (2016).
[19] A. J. Neukirch, W. Nie, J.-C. Blancon, K. Appavoo, H. Tsai, M. Y. Sfeir, C. Katan, L. Pedesseau, J. Even, J. J. Crochet, G. Gupta, A. D. Mohite, and S. Tretiak, Nano Lett. **16**, 3809 (2016).
[20] T. M. Brenner, D. A. Egger, A. M. Rappe, L. Kronik, G. Hodes, and D. Cahen, J. Phys. Chem. Lett. **6**, 4754 (2015).
[21] W. Nie, J.-C. Blancon, A. J. Neukirch, K. Appavoo, H. Tsai, M. Chhowalla, M. A. Alam, M. Y. Sfeir, C. Katan, J. Even, S. Tretiak, J. J. Crochet, G. Gupta, and A. D. Mohite, Nat. Commun. **7**, 11574 (2016).
[22] J. Even, L. Pedesseau, C. Katan, M. Kepenekian, J.-S. Lauret, D. Sapori, and E. Deleporte, J. Phys. Chem. C **119**, 10161 (2015).
[23] H. Zhou, Q. Chen, G. Li, S. Luo, T.-b. Song, H.-S. Duan, Z. Hong, J. You, Y. Liu, and Y. Yang, Science **345**, 542 (2014).
[24] W.-J. Yin, T. Shi, and Y. Yan, Appl. Phys. Lett. **104**, 063903 (2014).
[25] M. Shirayama, H. Kadowaki, T. Miyadera, T. Sugita, M. Tamakoshi, M. Kato, T. Fujiseki, D. Murata, S. Hara, T. N. Murakami, S. Fujimoto, M. Chikamatsu, and H. Fujiwara, Phys. Rev. Appl. **5**, 014012 (2016).
[26] J.-C. Blancon, W. Nie, A. J. Neukirch, G. Gupta, S. Tretiak, L. Cognet, A. D. Mohite, and J. J. Crochet, Adv. Funct. Mater. **26**, 4283 (2016).
[27] G. Giorgi, J.-I. Fujisawa, H. Segawa, and K. Yamashita, J. Phys. Chem. Lett. **4**, 4213 (2013).
[28] A. M. A. Leguy, P. Azarhoosh, M. I. Alonso, M. Campoy-Quiles, O. J. Weber, J. Yao, D. Bryant, M. T. Weller, J. Nelson, A. Walsh, M. van Schilfgaarde, and P. R. F. Barnes, Nanoscale **8**, 6317 (2016).
[29] D. O. Demchenko, N. Izyumskaya, M. Feneberg, V. Avrutin, Ü. Özgür, R. Goldhahn, and H. Morkoç, Phys. Rev. B **94**, 075206 (2016).
[30] R. L. Milot, G. E. Eperon, H. J. Snaith, M. B. Johnston, and L. M. Herz, Adv. Funct. Mater. **25**, 6218 (2015).

[31] Y. Yang, D. P. Ostrowski, R. M. France, K. Zhu, J. van de Lagemaat, J. M. Luther, and M. C. Beard, Nat Photonics **10**, 53 (2016).

[32] M. B. Price, J. Butkus, T. C. Jellicoe, A. Sadhanala, A. Briane, J. E. Halpert, K. Broch, J. M. Hodgkiss, R. H. Friend, and F. Deschler, Nat. Commun. **6**, 8420 (2015).

[33] A. Miyata, A. Mitioglu, P. Plochocka, O. Portugall, J. T.-W. Wang, S. D. Stranks, H. J. Snaith, and R. J. Nicholas, Nat. Phys. **11**, 582 (2015).

[34] V. D'Innocenzo, G. Grancini, M. J. P. Alcocer, A. R. S. Kandada, S. D. Stranks, M. M. Lee, G. Lanzani, H. J. Snaith, and A. Petrozza, Nat. Commun. **5**, 3586 (2014).

[35] M. E. Ziffer, J. C. Mohammed, and D. S. Ginger, ACS Photonics **3**, 1060 (2016).

[36] J. S. Manser and P. V. Kamat, Nat. Photonics **8**, 737 (2014).

[37] J. Even, L. Pedesseau, and C. Katan, J. Phys. Chem. C **118**, 11566 (2014).

[38] K. G. Stamplecoskie, J. S. Manser, and P. V. Kamat, Energy Environ. Sci. **8**, 208 (2015).

[39] R. T. Ross and A. J. Nozik, J. Appl. Phys. **53**, 3813 (1982).

[40] F. Zheng, L. Z. Tan, S. Liu, and A. M. Rappe, Nano Lett. **15**, 7794 (2015).

[41] D. Niesner, M. Wilhelm, I. Levchuk, A. Osvet, S. Shrestha, M. Batentschuk, C. Brabec, and T. Fauster, Phys. Rev. Lett. **117**, 126401 (2016).

[42] T. Etienne, E. Mosconi, and F. De Angelis, J. Phys. Chem. Lett. **7**, 1638 (2016).

[43] P. Azarhoosh, S. McKechnie, J. M. Frost, A. Walsh, and M. van Schilfgaarde, APL Mater. **4**, 091501 (2016).

[44] J. Ma and L.-W. Wang, Nano Lett. **15**, 248 (2015).

[45] H. Kawai, G. Giorgi, A. Marini, and K. Yamashita, Nano Lett. **15**, 3103 (2015).

[46] T. J. Savenije, C. S. Ponseca, L. Kunneman, M. Abdellah, K. Zheng, Y. Tian, Q. Zhu, S. E. Canton, I. G. Scheblykin, T. Pullerits, A. Yartsev, and V. Sundström, J. Phys. Chem. Lett. **5**, 2189 (2014).

[47] F. E. Camino, C.-Y. Nam, Y. T. Pang, J. Hoy, M. D. Eisaman, C. T. Black, and M. Y. Sfeir, J. Mod. Opt. **61**, 1735 (2014).

[48] C. Wehrenfennig, M. Liu, H. J. Snaith, M. B. Johnston, and L. M. Herz, APL Mater. **2**, 081513 (2014).

[49] J. Even, L. Pedesseau, J.-M. Jancu, and C. Katan, Phys. Status Solidi RRL **8**, 31 (2014).

[50] See Supplemental Material at http://link.aps.org/supplemental/10.1103/PhysRevB.96.195308 for (a) scanning electron micrographs of thin film of hybrid perovskite studied, (b) ultrafast dynamics when hybrid perovskite is optically pumped with 420 nm and 560 nm laser pulses, (c) representative curve fitting for the high-energy absorptive bleach bands at 250 K, 220 K, 150 K, 140 K and 100 K, (d) transient spectra extracted at 5 ps comparing thin film and bulk sample, (e) Energy diagrams explaining band folding effects from the cubic-reference phase to the low-temperature orthorhombic phase, (d) Symmetry analysis of the folding from the R and M points of the cubic phase to the Γ point of the orthorhombic phase.

[51] H. Wang, L. Whittaker-Brooks, and G. R. Fleming, J. Phys. Chem. C **119**, 19590 (2015).

[52] O. Yaffe, Y. Guo, L. Z. Tan, D. A. Egger, T. Hull, C. C. Stoumpos, F. Zheng, T. F. Heinz, L. Kronik, M. G. Kanatzidis, J. S. Owen, A. M. Rappe, M. A. Pimenta, and L. E. Brus, Phys. Rev. Lett. **118**, 136001 (2017).

[53] A. Y. Chang, Y.-J. Cho, K.-C. Chen, C.-W. Chen, A. Kinaci, B. T. Diroll, M. J. Wagner, M. K. Y. Chan, H.-W. Lin, and R. D. Schaller, Adv. Energy Mater. **6**, 1600422 (2016).

[54] W. Kong, Z. Ye, Z. Qi, B. Zhang, M. Wang, A. Rahimi-Iman, and H. Wu, Phys. Chem. Chem. Phys. **17**, 16405 (2015).

[55] A. M. A. Leguy, J. M. Frost, A. P. McMahon, V. G. Sakai, W. Kockelmann, C. Law, X. Li, F. Foglia, A. Walsh, B. C. O'Regan, J. Nelson, J. T. Cabral, and P. R. F. Barnes, Nat. Commun. **6**, 7124 (2015).

[56] T. Chen, B. J. Foley, B. Ipek, M. Tyagi, J. R. D. Copley, C. M. Brown, J. J. Choi, and S.-H. Lee, Phys. Chem. Chem. Phys. **17**, 31278 (2015).

[57] A. Olkhovets, R. C. Hsu, A. Lipovskii, and F. W. Wise, Phys. Rev. Lett. **81**, 3539 (1998).

[58] Y. P. Varshni, Physica **34**, 149 (1967).

[59] P. B. Allen and M. Cardona, Phys. Rev. B **27**, 4760 (1983).

[60] I. Kang and F. W. Wise, J. Opt. Soc. Am. B **14**, 1632 (1997).

[61] P. Umari, E. Mosconi, and F. De Angelis, Sci. Rep. **4**, 4467 (2014).

[62] F. Brivio, K. T. Butler, A. Walsh, and M. van Schilfgaarde, Phys. Rev. B **89**, 155204 (2014).

[63] A. D. Wright, C. Verdi, R. L. Milot, G. E. Eperon, M. A. Pérez-Osorio, H. J. Snaith, F. Giustino, M. B. Johnston, and L. M. Herz, Nat. Commun. **7**, 11755 (2016).

[64] K. Chen, A. J. Barker, F. L. C. Morgan, J. E. Halpert, and J. M. Hodgkiss, J. Phys. Chem. Lett. **6**, 153 (2015).

[65] A. Caretta, M. C. Donker, D. W. Perdok, D. Abbaszadeh, A. O. Polyakov, R. W. A. Havenith, T. T. M. Palstra, and P. H. M. van Loosdrecht, Phys. Rev. B **91**, 054111 (2015).

[66] M. Bernardi, J. Mustafa, J. B. Neaton, and S. G. Louie, Nat. Commun. **6**, 7044 (2015).

[67] M. L. Brongersma, N. J. Halas, and P. Nordlander, Nat. Nanotechnol. **10**, 25 (2015).

[68] M. W. Knight, H. Sobhani, P. Nordlander, and N. J. Halas, Science **332**, 702 (2011).

[69] B. Y. Zheng, H. Zhao, A. Manjavacas, M. McClain, P. Nordlander, and N. J. Halas, Nat. Commun. **6**, 7797 (2015).

[70] J. Urayama, T. B. Norris, J. Singh, and P. Bhattacharya, Phys. Rev. Lett. **86**, 4930 (2001).

[71] S. V. Kilina, D. S. Kilin, and O. V. Prezhdo, ACS Nano **3**, 93 (2009).

[72] X.-Q. Li, H. Nakayama, and Y. Arakawa, Phys. Rev. B **59**, 5069 (1999).

[73] W. A. Tisdale, K. J. Williams, B. A. Timp, D. J. Norris, E. S. Aydil, and X. Y. Zhu, Science **328**, 1543 (2010).